A Perfect Absorbing Layer for High-Order Simulation of Wave Scattering Problems

Li-Lian Wang and Zhiguo Yang

Abstract We report a novel approach to design artificial absorbing layers for spectral-element discretisation of wave scattering problems with bounded scatterers. It is essentially built upon two techniques: (i) a complex compression coordinate transformation that compresses all outgoing waves in the open space into the artificial layer, and then forces them to be attenuated and decay exponentially; (ii) a substitution (for the unknown) that removes the singularity induced by the transformation, and diminishes the oscillations near the inner boundary of the layer. As a result, the solution in the absorbing layer has no oscillation and is well-behaved for arbitrary high wavenumber and very thin layer. It is therefore well-suited and perfect for high-order simulations of scattering problems.

1 Introduction

Many partial differential equations (PDEs) are naturally set in unbounded domains. In order to solve them numerically, one has to truncate or reduce the infinite physical domains in some way. A critical issue is how to carry out this without inducing significant artificial errors to the solutions. A direct domain truncation with a hard-wall or periodic boundary condition is a viable option for problems with rapidly decaying solutions in space. For problems with decaying but slowly varying solutions (e.g., elliptic and diffusion equations), a reliable approach is to compress the solution at infinity to a finite domain by using a suitable coordinate transformation, and then solve the transformed PDE in a finite domain with a

L.-L. Wang (✉)
Division of Mathematical Sciences, School of Physical and Mathematical Sciences, Nanyang Technological University, Singapore 637371
e-mail: lilian@ntu.edu.sg

Z. Yang
Division of Mathematical Sciences, School of Physical and Mathematical Sciences, Nanyang Technological University, Singapore 637371

Present address: Department of Mathematics, Purdue University, West Lafayette, IN 47907, USA
e-mail: yang0347@e.ntu.edu.sg, yang1508@purdue.edu

M.L. Bittencourt et al. (eds.), *Spectral and High Order Methods for Partial Differential Equations ICOSAHOM 2016*, Lecture Notes in Computational Science and Engineering 119, DOI 10.1007/978-3-319-65870-4_5

hard-wall boundary condition. However, these techniques fail to work for wave problems as the underlying solutions are typically oscillating and decay slowly. Indeed, Johnson [13] remarked that "any real coordinate mapping from an infinite to a finite domain will result in solutions that oscillate infinitely fast as the boundary is approached – such fast oscillations cannot be represented by any finite-resolution grid, and will instead effectively form a reflecting hard wall." In practice, the reduction of an unbounded domain by artificial boundary conditions [12] and perfectly matched layers (PMLs) [3, 9] has been intensively studied for the scattering problems.

In this report, we offer a new absorbing layer that is well-suited for high-order discretisation of wave scattering problems. The idea stems from the concept of an inside-out (or inverse) invisibility cloak for electromagnetic waves, first proposed by Zharova et al. [18], which was based on a coordinate transformation that compresses an open space to a finite cloaking layer with physically meaningful medium. Such a layer was expected to prevent waves inside the enclosed region from propagating outside of the layer. Ideally, the cloaking layer could be a perfect absorbing layer for scattering problems. However, it was far from perfect, as the material parameters therein were highly singular and the approximation of the solution suffered from *the curse of infinite oscillation* [13]. We introduce two techniques to surmount these obstacles: (i) complex compression coordinate transformation; and (ii) variable substitution. This leads to a transformed problem in the absorbing layer with the remarkable features: (i) its solution has no oscillation; and (ii) it is nearly definite for arbitrary high wavenumber, as opposite to the strong indefiniteness of the Helmholtz and Maxwell's equations. To fix the idea, we focus on the two-dimensional Helmholtz problem with a circular absorbing layer, and outline the extension to the rectangular layer. We demonstrate that the proposed absorbing layer is completely non-reflective and perfect for very thin layer, arbitrary high wavenumber and incident angle.

It is noteworthy that (i) the idea of using complex transformations to damp the waves is similar to complex stretching of PMLs [3, 8–10], but the transformation herein compresses all outgoing waves into the layer, and also maps the far-field boundary condition to the outer boundary naturally; and (ii) the use of substitution $u = ve^{\mathrm{i}k\rho}/\sqrt{\rho}$ is found in the context of infinite element methods for scattering problems to capture the decay rate of outgoing wave, see e.g., [11], but the substitution in (20) is adopted for different purpose with a different power in ρ.

2 Time-Harmonic Acoustic Scattering Problem

Consider the time-harmonic wave scattering governed by the Helmholtz equation:

$$\Delta u + k^2 u = 0 \quad \text{in} \;\; \Omega_\infty := \mathbb{R}^2 \setminus \bar{D}; \tag{1a}$$

$$u = g \quad \text{on} \;\; \partial D; \quad \partial_r u - \mathrm{i}ku = o(r^{-1/2}) \;\; \text{as} \;\; r = |\mathbf{x}| \to \infty, \tag{1b}$$

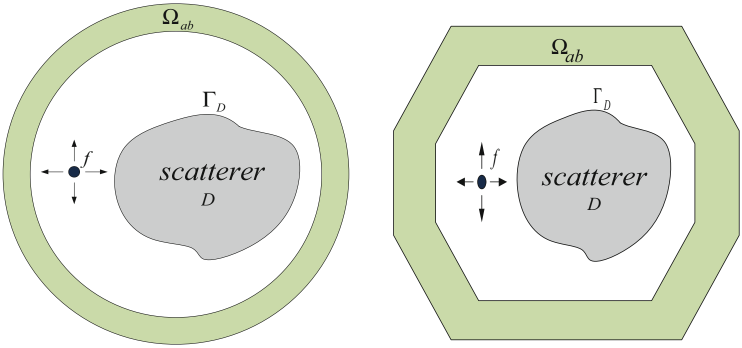

Fig. 1 Schematic illustration of an absorbing layer $\Omega_{\rm ab}$. *Left*: annular layer. *Right*: polygonal layer

where the wavenumber $k > 0$, $D \subset \mathbb{R}^2$ is a bounded scatterer with Lipschitz boundary $\Gamma_D = \partial D$, and the data $g \in H^{1/2}(\Gamma_D)$ is generated by the incident wave. In fact, the technique can be applied to solve the Helmholtz-type problems in inhomogeneous, anisotropic media or with an external source, which are confined in a bounded domain Ω_a enclosing $\bar{D}$, that is,

$$\nabla \cdot \big(\mathbf{C}\, \nabla u\big) + k^2 n\, u = f \quad \text{in} \;\; \Omega_\infty, \tag{2}$$

in place of (1a). Here, $\mathbf{C} \in \mathbb{C}^{2\times 2}$ is a symmetric matrix, and $n > 0$ the reflective index. Assume that exterior to Ω_a, $\mathbf{C} = \mathbf{I}_2, n = 1$ and $f = 0$.

To numerically solve the exterior problem (1) or (2) with (1b), we reduce the infinite domain by surrounding the computational domain $\Omega_f := \Omega_a \setminus \bar{D}$ via an artificial layer $\Omega_{\rm ab}$ with a finite thickness. Without loss of generality, we consider two types of layers: (i) $\Omega_{\rm ab} = \{a < r < b\}$ is a circular annulus (cf. Fig. 1 (left)); and (ii) $\Omega_{\rm ab}$ is a polygonal annulus (cf. Fig. 1 (right)). The former is more convenient to illustrate the idea and to compare with the PML techniques in [3, 7, 10], while the latter is more practical and flexible to the geometry of the scatterer. In what follows, we focus on the derivation of the PDE in $\Omega_{\rm ab}$ that couples with the Helmholtz problem in Ω_f to achieve the aforementioned goals.

The form of the transformed Helmholtz operator under a generic coordinate transformation finds useful later on, which can be verified by knowledge of calculus.

Lemma 1 *Define the Helmholtz operator:*

$$\tilde{\mathscr{H}}[\tilde{u}] = \Delta \tilde{u} + k^2 \tilde{u}. \tag{3}$$

Given a coordinate transformation between $\tilde{\mathbf{x}} = (\tilde{x}, \tilde{y})$ *and* $\mathbf{x} = (x, y)$ *with the Jacobian matrix*

$$x = x(\tilde{\mathbf{x}}), \quad y = y(\tilde{\mathbf{x}}); \quad \mathbf{J} := \frac{\partial(x,y)}{\partial(\tilde{x},\tilde{y})} = \begin{bmatrix} \partial_{\tilde{x}} x \; \partial_{\tilde{y}} x \\ \partial_{\tilde{x}} y \; \partial_{\tilde{y}} y \end{bmatrix}, \tag{4}$$

we have the transformed Helmholtz operator

$$\mathscr{H}[u] = \frac{1}{n}\{\nabla \cdot \big(\mathbf{C}\nabla u\big) + k^2 n\, u\}, \tag{5}$$

where $u(\mathbf{x}) = \tilde{u}(\tilde{\mathbf{x}})$ *and*

$$\mathbf{C} = \begin{bmatrix} C_{11} & C_{12} \\ C_{12} & C_{22} \end{bmatrix} = \frac{\mathbf{J}\,\mathbf{J}^t}{\det(\mathbf{J})}, \quad n = \frac{1}{\det(\mathbf{J})}. \tag{6}$$

2.1 Real Compression Coordinate Transformation

We start with the "compression" coordinate transformation for the inside-out invisibility cloak in [18]:

$$r = b - \frac{(b-a)^2}{\rho + b - 2a} \quad \text{or} \quad \rho = \frac{s(r)}{b-r}, \quad s(r) := a^2 + r(b-2a), \tag{7}$$

for $\rho \in [a, \infty)$ and $r \in [a, b)$. This one-to-one mapping compresses the open space exterior to a disk of radius $\rho = a$ into the annulus $a \le r < b$, where the inner circle $\rho = a (= r)$ remains unchanged, while $\rho = \infty$ corresponds to $r = b$.

We now derive the equation in the compressed layer $\Omega_{\rm ab}$ by using Lemma 1. By the chain rule involving the original Cartesian coordinates-$(\tilde{x}, \tilde{y})$ with the polar coordinates-(ρ, θ); and the physical Cartesian coordinates-(x, y) with the polar coordinates-(r, θ), we have

$$\mathbf{J} = \frac{\partial(x,y)}{\partial(\tilde{x},\tilde{y})} = \frac{\partial(x,y)}{\partial(r,\theta)}\frac{\partial(r,\theta)}{\partial(\rho,\theta)}\frac{\partial(\rho,\theta)}{\partial(\tilde{x},\tilde{y})}. \tag{8}$$

A direct calculation leads to

$$\mathbf{J} = \mathbf{R}\,\mathbf{J}_0\,\mathbf{R}^t \quad \text{with} \quad \mathbf{J}_0 = \begin{bmatrix} dr/d\rho & 0 \\ 0 & r/\rho \end{bmatrix}, \quad \mathbf{R} = \begin{bmatrix} \cos\theta & -\sin\theta \\ \sin\theta & \cos\theta \end{bmatrix}. \tag{9}$$

Then by (6),

$$\mathbf{C}_0 = \mathbf{R}\begin{bmatrix} c_0 & 0 \\ 0 & 1/c_0 \end{bmatrix}\mathbf{R}^t, \quad n_0 = \frac{\rho}{r}\frac{d\rho}{dr}, \quad c_0 := \frac{\rho}{r}\frac{dr}{d\rho}. \tag{10}$$

As a consequence of Lemma 1, we obtain the modified Helmholtz equation:

$$\nabla \cdot \big(\mathbf{C}_0\nabla u\big) + k^2 n_0\, u = 0 \quad \text{in} \;\; \Omega_{ab}. \tag{11}$$

Noting from (7) that

$$\frac{d\rho}{dr} = \Big(\frac{b-a}{b-r}\Big)^2 = \Big(\frac{dr}{d\rho}\Big)^{-1}, \quad r \in (a,b), \tag{12}$$

we have

$$n_0 = \frac{s(r)}{r}\frac{(b-a)^2}{(b-r)^3}, \quad c_0 = \frac{s(r)}{r}\frac{b-r}{(b-a)^2}. \tag{13}$$

It is evident that $1/c_0, n \to \infty$, when $r \to b^-$. This implies the wavenumber becomes infinitely large near the outer boundary of layer $\Omega_{\rm ab}$. In other words, the solution u has infinite oscillation. It is no wonder that all the outgoing waves in the open space are compressed into the finite layer $\Omega_{\rm ab}$, so this induces the so-called *curse of infinite oscillation*. Thus, it is advisable to use a *complex compression coordinate transformation* to attenuate the waves.

2.2 Complex Compression Coordinate Transformation

Different from (7), we introduce the complex compression mapping

$$\tilde\rho(r) = \rho(r) + {\rm i}\sigma_0(\rho(r) - a), \quad \rho(r) = \frac{s(r)}{b-r}, \quad r \in [a,b), \tag{14}$$

where $s(r) = a^2 + r(b-2a)$ as before, and $\sigma_0 > 0$ is a tuning parameter. For notational convenience, we denote

$$\alpha := 1 + {\rm i}\sigma_0 = \frac{d\tilde\rho}{d\rho}, \quad \beta := 1 + {\rm i}\sigma_0\Big(1 - \frac{a}{\rho}\Big) = \frac{\tilde\rho}{\rho}. \tag{15}$$

Using Lemma 1, we can derive following PDE in $\Omega_{\rm ab}$.

Theorem 1 *Using the transformation* (14)*, we derive the Helmholtz-type problem:*

$$\nabla\cdot\big(\mathbf{C}\nabla u\big) + k^2\, n\, u = 0 \quad \text{in} \ \ \Omega_{ab}, \tag{16}$$

$$u = \Psi \quad \text{at} \ \ r = a; \quad \frac{1}{\alpha}\frac{dr}{d\rho}\partial_r u - {\rm i}ku = o(|\tilde\rho|^{-1/2}) \ \ \text{as} \ \ r \to b^-, \tag{17}$$

where Ψ *is from the solution of the interior Helmholtz equation at the inner boundary* $r = a$*, and*

$$\mathbf{C} = \mathbf{R}\begin{bmatrix} c & 0 \\ 0 & 1/c \end{bmatrix}\mathbf{R}^t, \quad n = \alpha\beta\frac{s(r)}{r}\frac{(b-a)^2}{(b-r)^3}, \quad c = \frac{\beta}{\alpha}\frac{s(r)}{r}\frac{b-r}{(b-a)^2}. \tag{18}$$

Moreover, if $\psi \in L^2(0, 2\pi)$*, we have the following point-wise bounds for all* $r \in (a, b)$,

$$\|u(r,\cdot)\|_{L^2(0,2\pi)} \le \exp\Big\{-k\sigma_0(\rho-a)\Big(1-\frac{a^2}{k^2\rho^2+k^2\sigma_0^2(\rho-a)^2}\Big)^{1/2}\Big\}\|\Psi\|_{L^2(0,2\pi)}. \tag{19}$$

It is important to point out that the solution in the point-wise sense (19) decays exponentially like $O(e^{-k\sigma_0/(b-r)})$ as $r \to b^-$. We also observe from (18) that the coefficients $1/c, n \to \infty$ as $r \to b^-$. Though the product nu is well-behaved, the problem (16)–(17) is still challenging for numerical solution due to the involved singular coefficients.

2.3 Variable Substitution

To handle the singularity and remove essential oscillations of u, we introduce the following substitution in $\Omega_{\rm ab}$:

$$u = vw, \quad w = \Big(\frac{a}{\rho}\Big)^{3/2} e^{{\rm i}k(\rho-a)}, \tag{20}$$

where $\rho = \rho(r)$ is as in (7). It is important to remark that

(i) We incorporate the complex exponential to capture the oscillation of u, so that v essentially has no oscillation for arbitrary high wavenumber and very thin layer (see Fig. 2 below).

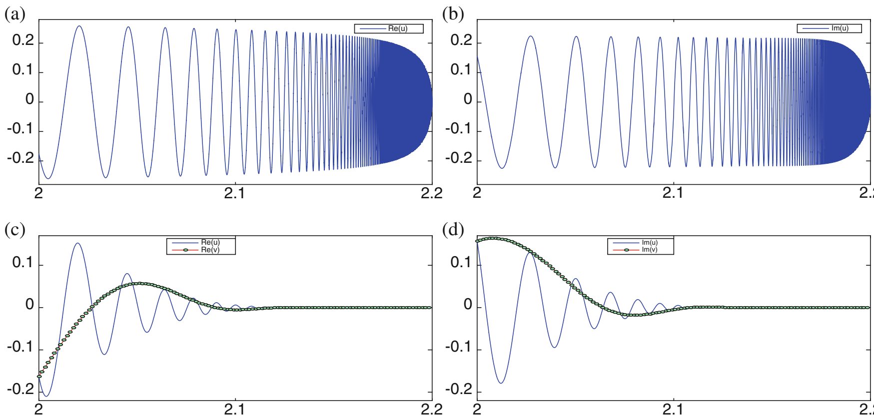

Fig. 2 Profiles of the solution (33) with $k = 200$, $\theta_0 = \pi/4$ and $a_0 = 1$ under the real compression mapping (7) and complex compression mapping (14), and the substitution (20) with $r \in (2, 2.2)$ and along $\theta = 0$. (**a**) ${\rm Re}\{u(\rho(r), 0)\}$ under (7). (**b**) ${\rm Im}\{u(\rho(r), 0)\}$ under (7). (**c**) ${\rm Re}\{u(\tilde\rho(r), 0)\}$ under (14) vs. ${\rm Re}\{v\}$ in (20). (**d**) ${\rm Im}\{u(\tilde\rho(r), 0)\}$ under (14) vs. ${\rm Im}\{v\}$ in (20)

(ii) In real implementation, we can build in the substitution into the basis functions, and formally approximate u by non-conventional basis:

$$u_N \in \operatorname{span}\big\{\psi_j = w\phi_j \,:\, 0 \le j \le N\big\}, \tag{21}$$

where v is essentially approximated by the usual polynomial or piecewise polynomial basis $\{\phi_j\}$ in spectral/spectral-element methods.

Remark 1 Recall that for fixed m and large $|z|$ (cf. [1]),

$$H_m^{(1)}(z) \sim \sqrt{\frac{2}{\pi z}}\, e^{\mathrm{i}(z-\frac{1}{2}m\pi-\frac{1}{4}\pi)}, \quad -\pi < \arg(z) < 2\pi. \tag{22}$$

By (60), we have the asymptotic estimates for fixed m :

$$|\hat{u}_m(r)| = |\hat{\psi}_m| \Big|\frac{H_m^{(1)}\big(k\tilde{\rho}(r)\big)}{H_m^{(1)}(ka)}\Big| \sim \sqrt{\frac{a}{|\tilde{\rho}|}} e^{-k\sigma_0(\rho-a)} |\hat{\psi}_m|\, e^{\mathrm{i}k(\rho-a)}. \tag{23}$$

In view of this, the complex exponential in (20) captures the oscillations of u near the inner boundary $r = a$, so we expect v has no oscillation and decays exponentially in the layer $\Omega_{\rm ab}$. □

We find it is more convenient to carry out the substitution through the variational form. Let $L^2_\omega(\Omega)$ be a weighted space of square integrable functions with the inner product and norm denoted by $(\cdot,\cdot)_{\omega,\Omega}$ and $\|\cdot\|_{\omega,\Omega}$ as usual. Define the trace integral $\langle u, v\rangle_{\Gamma_b} := \oint_{\Gamma_b} u\, \bar{v}\, \mathrm{d}\gamma$. Let $\Omega = \Omega_f \cup \Omega_{\rm ab}$, and assume $g = 0$. Formally, we define the bilinear form associated with (1) in Ω_f coupled with (16):

$$\mathbb{B}_\Omega(u,\phi) := \mathbb{B}_{\Omega_f}(u,\phi) + \mathbb{B}_{\Omega_{\rm ab}}(u,\phi) \quad \text{with} \quad \mathbb{B}_{\Omega_f}(u,\phi) = (\nabla u, \nabla\phi)_{\Omega_f} - k^2(u,\phi)_{\Omega_f},$$

$$\mathbb{B}_{\Omega_{\rm ab}}(u,\phi) = (\mathbf{C}\nabla u, \nabla\phi)_{\Omega_{\rm ab}} - k^2(n\,u,\phi)_{\Omega_{\rm ab}} - \langle \mathbf{C}\nabla u\cdot\mathbf{n}, \phi\rangle_{\Gamma_b}, \tag{24}$$

where $\mathbf{n} = (\cos\theta, \sin\theta)^t$ is the unit outer normal to Γ_b.

Theorem 2 *With the substitution $u = vw$ and $\phi = \psi w$ in (20), we have*

$$\mathbb{B}_{\Omega_{\rm ab}}(u,\phi) = \big(\varpi_1 \mathbf{C}\nabla v, \nabla\psi\big)_{\Omega_{\rm ab}} + \frac{1}{\alpha}\big(\beta\partial_{\mathbf{n}} v, \psi\varpi_2\big)_{\Omega_{\rm ab}} + \frac{1}{\alpha}\big(\beta\varpi_2 v, \partial_{\mathbf{n}}\psi\big)_{\Omega_{\rm ab}} + \big(\varpi_3 v, \psi\big)_{\Omega_{\rm ab}}, \tag{25}$$

where $\partial_{\mathbf{n}} = \mathbf{n}\cdot\nabla$ is the directional derivative along the normal direction, and

$$\varpi_1 = \frac{a^3}{\rho^3}, \quad \varpi_2 = \frac{a^3}{r}\frac{1}{\rho^2}\Big(-\frac{3}{2\rho} + \mathrm{i}k\Big), \quad \varpi_3 = \frac{a^3(b-a)^2}{rs^2(r)}\Big(\Big(\frac{\beta}{\alpha} - \alpha\beta\Big)k^2 + \frac{\beta}{\alpha}\frac{9}{4\rho^2}\Big),$$

$$\alpha = 1 + \mathrm{i}\sigma_0, \quad \beta = 1 + \mathrm{i}\sigma_0\Big(1 - \frac{a}{\rho}\Big), \quad \frac{1}{\rho} = \frac{b-r}{s(r)}, \quad s(r) = a^2 + r(b-2a), \quad r \in (a,b). \tag{26}$$

Remark 2 Some remarks are in order.

(i) Compared with the singular coefficients in (18), we observe from (26) that the involved coefficients become regular. In particular, ϖ_3 is uniformly bounded above and below away from zero.
(ii) The DtN boundary condition is transformed to the outer boundary $r = b$, this naturally eliminate the boundary term in (24).
(iii) When u is approximated by a non-conventional basis (21), we can use (25)–(26) to compute the matrices of the linear system. In fact, $\Omega_{\rm ab}$ can be replaced by any element of a non-overlapping partition of $\Omega_{\rm ab}$. □

Remarkably, the transformed problem in v is nearly definite for any wavenumber $k > 0$, as opposite to the indefiniteness of the original problem.

Theorem 3 *With the substitution $u = vw$ in (20), we have*

$$\begin{aligned}\mathrm{Re}\big\{\mathbb{B}_{\Omega_{\rm ab}}(u,u)\big\} \ge & c_1(1-\epsilon^{-1})\|\partial_r v\|^2_{\omega^2} + c_2\|\partial_\theta v\|^2_{\omega} + c_3\|v(a,\cdot)\|^2_{L^2(0,2\pi)} \\ & + a^3|I|^2k^2\int_0^{2\pi}\!\!\int_a^b \frac{\Theta(r)}{s^2(r)}|v|^2 drd\theta,\end{aligned} \tag{27}$$

where $\omega = b - r$, $|I| = b - a$, $\varepsilon > 1$ and

$$c_1 = \frac{a^3}{b\bar{c}^2|I|^4}\frac{1}{1+\sigma_0^2}, \quad c_2 = \frac{a^3}{b\bar{c}^4|I|^2}, \quad c_3 = \frac{3}{2}\frac{1}{1+\sigma_0^2}, \quad \bar{c} = \max\{a, |I|\},$$
$$\Theta(r) = \frac{15}{4a^2k^2}\frac{\sigma_0^2}{1+\sigma_0^2}t^3 - \frac{9}{4a^2k^2}t^2 - \frac{\sigma_0^2}{1+\sigma_0^2}\big(\sigma_0^2 - \epsilon + 2\big)t + (\sigma_0^2 - \epsilon), \quad t = \frac{a}{\rho}. \tag{28}$$

For simplicity, we denote the coefficients (up to a sign) of the cubic polynomial in t by $\{\gamma_i\}_{i=0}^3$, and define

$$\widetilde{\Theta}(t) := \Theta(r) = \gamma_3 t^3 - \gamma_2 t^2 - \gamma_1 t + \gamma_0, \quad t \in (0, 1]. \tag{29}$$

One verifies readily that

$$\widetilde{\Theta}'(t) = 3\gamma_3\Big\{\Big(t - \frac{\gamma_2}{3\gamma_3}\Big)^2 - \frac{\gamma_2^2}{9\gamma_3^2} - \frac{\gamma_1}{3\gamma_3}\Big\}, \quad \frac{\gamma_2}{3\gamma_3} = \frac{1+\sigma_0^2}{5\sigma_0},$$
$$\widetilde{\Theta}'(0) = -\gamma_1 < 0, \quad \widetilde{\Theta}'(1) < 3\gamma_3\Big(\frac{3}{5} - \frac{4a^2k^2}{45}\big(\sigma_0^2 - \epsilon + 2\big)\Big).$$

If $k^2 \ge k_0^2 := 27/(4a^2(\sigma_0^2 - \epsilon + 2))$ and $1 < \epsilon < \sigma_0^2$, then $\widetilde{\Theta}'(t) < 0$, and

$$\widetilde{\Theta}(1) < \widetilde{\Theta}(t) < \widetilde{\Theta}(0) = \sigma_0^2 - \epsilon, \quad t \in (0, 1); \quad \widetilde{\Theta}(t) \ge \widetilde{\Theta}(t_*) > 0, \quad t \in (0, t_*], \tag{30}$$

where

$$t_* = \frac{\gamma_0}{\gamma_1} = 1 - \frac{1+\epsilon\sigma_0^{-2}}{1+(2-\epsilon)\sigma_0^{-2}}\frac{1}{\sigma_0^2}, \quad t_* = 1 - \frac{1}{\sigma_0^2} + 2(\epsilon-1)\frac{1}{\sigma_0^4} + O(\sigma_0^{-6}). \tag{31}$$

This implies

$$\Theta(r) > 0 \quad \text{if} \quad \rho \geq \frac{a}{t_*} \quad \text{or} \quad a < \frac{b-a+b(t_*^{-1}-1)}{b-a+a(t_*^{-1}-1)}a \leq r < b. \tag{32}$$

In particular, if $\sigma_0 \gg 1$, we have $\Theta(r) > 0$ for all $r \in (a,b)$.

2.4 Numerical Results

2.4.1 Illustration of the Solution in Ω_{ab} Under Different Transformations

Consider the exterior problem

$$\Delta u + k^2 u = 0, \quad \rho > a_0; \quad u|_{\rho=a_0} = g; \quad \partial_\rho u - \mathrm{i}ku = o(\rho^{-1/2}), \tag{33}$$

where we take $g = -\exp\big(\mathrm{i}ka_0\cos(\theta-\theta_0)\big)$ with the incident angle θ_0. It is known that it admits a unique series solution $u(\rho,\theta)$. As before, we reduce the unbounded domain by an artificial annular layer Ω_{ab} with radius $a > a_0$.

We plot in Fig. 2 the profiles of the solution under different transformations. We see that the infinite oscillation of the solution in the layer Ω_{ab} by the real compression transformation (7). The solution decays exponentially with the complex compression transformation, but it oscillates near $r = a$. However, with the substitution (20), v becomes well-behaved in the layer, which actually we approximate.

2.4.2 Spectral-Element Methods for Scattering Problems

We demonstrate that the proposed absorbing layer is totally non-reflective, and robust for high wavenumber and very thin layer. To show the high accuracy, we solve (1) with the scatterer D being a disk of radius a_0, which is reduced to two annuluses: $\Omega = \Omega_f \cup \Omega_{ab}$. Here, we use Fourier approximation in θ direction, and spectral-element method in radial direction [14]. Note that for $r \in [a,b]$, we use the non-standard basis $\psi_j = w\phi_j$ with ϕ_j being the usual polynomial nodal or modal basis as in (21).

We also intend to compare our approach with the PML technique using the complex coordinate stretching

$$\tilde{r} = r + \mathrm{i}\int_a^r \sigma(t)dt, \quad r \in (a,b), \quad \sigma(t) > 0. \tag{34}$$

Typically, there are two choices of the absorbing function $\sigma(t)$.

(i) Regular function (see, e.g., [7, 10]):

$$\sigma(t) = \sigma_1\Big(\frac{t-a}{b-a}\Big)^n, \quad \text{so} \quad \tilde{r} = r + \mathrm{i}\,\sigma_1\,\frac{b-a}{n+1}\Big(\frac{r-a}{b-a}\Big)^{n+1}, \quad r \in (a,b), \tag{35}$$

where n is a positive integer and $\sigma_1 > 0$ is a tuning parameter.

(ii) Singular function (or unbounded absorbing function (see, e.g., [4, 5]):

$$\sigma(t) = \frac{\sigma_2}{b-t}, \quad \text{so} \quad \tilde{r} = r + \mathrm{i}\,\sigma_2 \ln\Big(\frac{b-a}{b-r}\Big), \quad r \in (a,b), \tag{36}$$

where $\sigma_2 > 0$ plays the same role as σ_1.

Observe from (14) and (36) that the imaginary parts of both transformations involve two different one-to-one mappings between $(0,\infty)$ and (a,b), i.e.,

$$z = \frac{\rho(r)-a}{b-a} = \frac{r-a}{b-r}, \quad r = \frac{a+bz}{1+z}, \quad r \in (a,b), \quad z \in (0,\infty), \tag{37}$$

and

$$z = \ln\Big(\frac{b-a}{b-r}\Big), \quad r = b - (b-a)\,\frac{1}{e^z}, \quad r \in (a,b), \quad z \in (0,\infty). \tag{38}$$

It is noteworthy that the algebraic mapping (37) has been used for mapped spectral methods in unbounded domains see, e.g., [6, 14], where at times one employs the following logarithmic mapping similar to (38):

$$z = \ln\Big(\frac{b-2a+r}{b-r}\Big), \quad r = b-(b-a)\frac{2}{1+e^z}, \quad r \in (a,b), \quad z \in (0,\infty). \tag{39}$$

Indeed, one can choose any of these singular mappings in (35) for the PML, but the singularity of the coefficients in the PML equation is very different between (38)–(39) and (37). In fact, the authors [4, 5] suggested the use of e.g., Gauss-quadrature rules to avoid sampling the singular values at $r = b$, but it should be pointed out the logarithmic singularity induced by (38) is more challenging to deal with than the algebraic mapping (37).

We reiterate the significant differences of our approach from the PML: (i) we use the compression transformation for both the real and imaginary parts in (36) so we can directly transform the far-field radiation conditions to $r = b$; and (ii) more importantly, the substitution allows us to remove the singularity and oscillation in the layer leading to well-behaved functions which can be accurately approximated by standard approximation tools.

In the test, we take g to be the same as in (33) with $a_0 = 1, \theta_0 = 0$, and use Theorem 2 to compute the matrices related to the artificial layer. Let M be the cut-off number of the Fourier modes, and $\mathbf{N} = (N_1, N)$ be the number of points in r-direction of two layers, respectively. We measure the maximum pointwise error in Ω_f. We take $N_1 = 200, M = ka$ with $a = 2$, $b = 2.2$ and vary N so that the waves in the interior layer can be well-resolved, and the error should be dominated by the approximation in the outer annulus. In Fig. 3a–b, we compare the accuracy of the solver with PAL ($\sigma_0 = 1.5$), PML ($n = 1, \sigma_1 = 1.89, 1.43$ for $k = 150, 200$, respectively: optimal value based on the rule in [7]) and UPML using unbounded absorbing function (36) ($\sigma_2 = 1/k$: optimal value suggested by [5]). Observe that our approach outperforms the PML with two choices of the absorbing functions, and the advantage is even significant for high wavenumber. In addition, the effect of the singularity related to UPML is observable for slightly large N.

We also study the influence of the thickness of the absorbing layer. In Fig. 3c, we vary the thickness of the layer $b - a = 0.02, 0.05, 0.1, 0.5$ and plot the error against $N = 5, 10, \cdots, 40$ with $k = 100$. For a fixed N, we observe the thinner the layer the smaller the error, which shows the result is insensitive to the thickness. In Fig. 3d, we plot $\mathrm{Re}(u_{\mathbf{N}})|_{\Omega_f}$ and $\mathrm{Re}(v_{\mathbf{N}})|_{\Omega_{\rm ab}}$ with $b - a = 0.02$ and $N = 40$. Notice that the approximation of v has no oscillation and is well-behaved in the layer.

In Fig. 3e–f, we further test PAL with a perfect conducting ellipse D with $\partial D := \{(x, y) = \zeta(\cosh\xi \cos\theta, \sinh\xi \sin\theta), \theta \in [0, 2\pi)\}$ and fix $(\zeta, \xi) = (0.8, 0.5)$ with $k = 50$, $(a, b) = (2, 2.2)$. We partition $\Omega = \{\Omega_f^{(i)}\}_{i=1}^8 \cup \{\Omega_{\rm ab}^{(i)}\}_{i=1}^8$ into 16 non-overlapping (curved) quadrilateral elements as shown in Fig. 3e. Using the Gordon-Hall elemental transformation $\{T_f^i, T_{\rm ab}^i\} : [-1, 1]^2 \mapsto \{\Omega_f^{(i)}, \Omega_{\rm ab}^{(i)}\}$, we define the

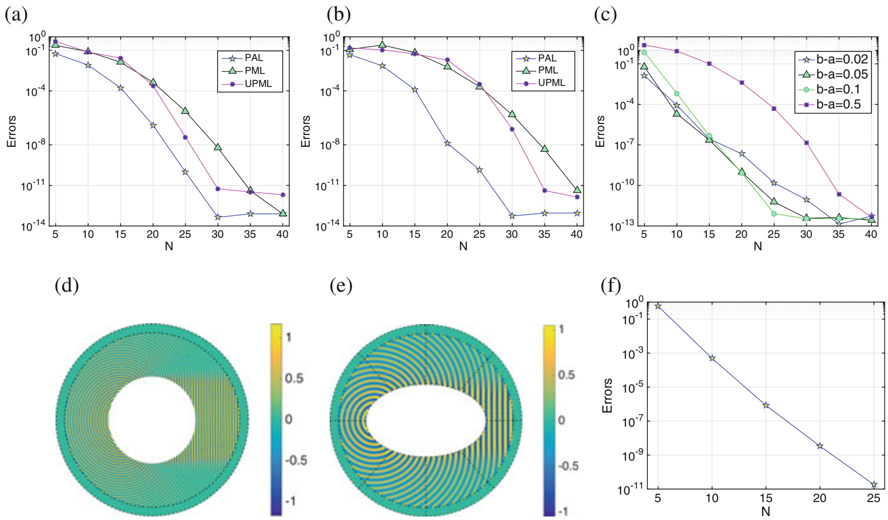

Fig. 3 In (**a**)–(**b**): $b = 2.2$. In (**c**): $k = 100$. In (**d**): $k = 100, b = 2.2, N = 40$. In (**e**)–(**f**): $k = 50, N_1 = 60$, $(a, b) = (2, 2.2)$, $\partial D := \{(x, y) = \zeta(\cosh\xi \cos\theta, \sinh\xi \sin\theta), \theta \in [0, 2\pi)\}$ with $(\zeta, \xi) = (0.8, 0.5)$, $\sigma_0 = 1.5$, and for (**e**): $N = 25$. (**a**) PAL vs PML ($k = 150$). (**b**) PAL vs PML ($k = 200$). (**c**) Errors vs thickness of $\Omega_{\rm ab}$. (**d**) $\mathrm{Re}(u_N)$ and $\mathrm{Re}(v_{\mathbf{N}})$. (**e**) $\mathrm{Re}(u_N)$ and $\mathrm{Re}(v_{\mathbf{N}})$. (**f**) Error of (**e**) against N

approximation space

$$u_{\mathbf{N}} \in V_{\mathbf{N}} = \Big\{ u \in H^1(\Omega) : u|_{\Omega_f^{(i)}} \circ T_f^i \in \mathbb{P}_{N_1} \times \mathbb{P}_{N_1},\ u|_{\Omega_{\rm ab}^{(i)}} = v_{\mathbf{N}} w,\ v_{\mathbf{N}}|_{\Omega_{\rm ab}^{(i)}} \circ T_{\rm ab}^i \in \mathbb{P}_{N_1} \times \mathbb{P}_N \Big\}. \tag{40}$$

In Fig. 3e, we plot $\mathrm{Re}(u_{\mathbf{N}})|_{\Omega_f}$ and $\mathrm{Re}(v_{\mathbf{N}})|_{\Omega_{\rm ab}}$ with $(N_1, N) = (60, 25)$. In Fig. 3f, we take $N_1 = 60$ (the interior layer can be well-resolved) and vary $N = 5, 10, \cdots, 25$ so that the maximum point-wise error in Ω_f should be dominated by N (the number of points along the radial direction in $\Omega_{\rm ab}$). We see the errors decay exponentially for the spectral-element approximation, and a high accuracy can be achieved with a small N.

2.4.3 Simulation of Cylindrical Inside-Out Cloak

We illustrate that with the lossy and dispersive materials in the cloaking layer $\Omega_{\rm ab}$, we can achieve the perfectness of the aforementioned inside-out cloak. Assume that the scatterer D in (1) is penetrable, and place an active "point" source centred at (x_0, y_0) in the disk $r < a$:

$$f(x, y) = A \exp\Big(- \frac{(x - x_0)^2 + (y - y_0)^2}{2\sigma^2} \Big), \tag{41}$$

with $(A, x_0, y_0, \sigma) = (10^5, -0.3, -0.3, 0.01)$. We take $k = 50$, $(a, b) = (1, 1.5)$ and $\sigma_0 = 0.1$. In Fig. 4a, we plot $\mathrm{Re}(u)|_{\Omega_f}$ and $\mathrm{Re}(v)|_{\Omega_{\rm ab}}$ with $(N_1, N) = (50, 30)$. We depict in Fig. 4b–c the extracted profiles along x-axis. We see that the waves radiated by the active source are completely absorbed by the cloaking layer $\Omega_{\rm ab}$. Indeed, the unknown v in the layer is very well-behaved.

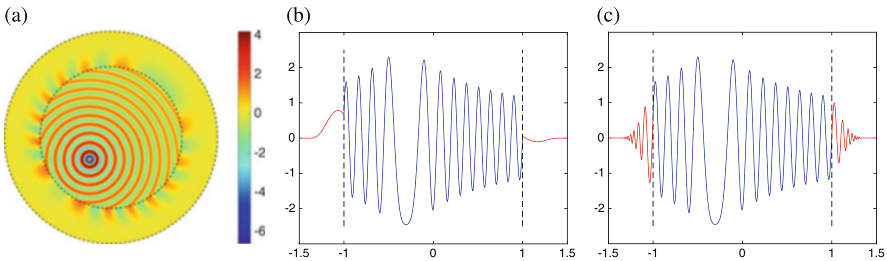

Fig. 4 Inside-out cloaking phenomenon generated by a point source defined in (41) with $k = 50$, $(a, b) = (1, 1.5)$, $\sigma_0 = 0.1$, $M = ka$ and $\mathbf{N} = (50, 30)$. (**a**) Cloaking of a point source. (**b**) Profile of u & v along x-axis. (**c**) Profile of u along x-axis

3 Rectangular/Polygonal Absorbing Layer

In practice, the rectangular/polygonal layer is more desirable and flexible for e.g., elongated scatterers and for element methods. In fact, the two techniques for designing the perfect annular absorbing layer can be extended to this setting. To fix the idea, we set

$$\Omega_f = \{\mathbf{x} \in \mathbb{R}^2 : |x_i| < L_i,\ i = 1, 2\}, \quad \Omega = \{\mathbf{x} \in \mathbb{R}^2 : |x_i| < L_i + d_i,\ i = 1, 2\},$$

with $L_1/L_2 = d_1/d_2$. Then, the absorbing layer consists of four trapezoidal pieces: $\Omega_{\rm ab} = \Omega \setminus \bar{\Omega}_f = \Omega^r \cup \Omega^l \cup \Omega^t \cup \Omega^b$, whose non-parallel sides are rays from the origin O, as illustrated in Fig. 5a.

Like (14), the complex compression coordinate transformation for the right and top pieces Ω^r and Ω^t, respectively, takes the form:

$$\tilde{x}_1 = \rho_1(x_1) + {\rm i}\sigma_0(\rho_1(x_1) - L_1), \quad \tilde{x}_2 = \tilde{x}_1 x_2/x_1, \quad \mathbf{x} \in \Omega^r, \tag{42}$$

$$\tilde{x}_2 = \rho_2(x_2) + {\rm i}\sigma_0(\rho_2(x_2) - L_2), \quad \tilde{x}_1 = \tilde{x}_2 x_1/x_2, \quad \mathbf{x} \in \Omega^t, \tag{43}$$

and for the left and bottom pieces Ω^r and Ω^t, we transform by symmetry:

$$\big(\tilde{x}_1(x_1), \tilde{x}_2(x_1, x_2)\big)\big|_{\Omega^l} = \big(-\tilde{x}_1(-x_1), \tilde{x}_2(-x_1, x_2)\big)\big|_{\Omega^r}, \tag{44}$$

$$\big(\tilde{x}_1(x_1, x_2), \tilde{x}_2(x_2)\big)\big|_{\Omega^b} = \big(\tilde{x}_1(x_1, -x_2), -\tilde{x}_2(-x_2)\big)\big|_{\Omega^t}. \tag{45}$$

In the above, we have

$$\rho_1(x_1) = \frac{L_1^2 + (d_1 - L_1)x_1}{L_1 + d_1 - x_1}, \quad \rho_2(x_2) = \frac{L_2^2 + (d_2 - L_2)x_2}{L_2 + d_2 - x_2}. \tag{46}$$

Like (7), the real transformation $\check{x}_1 = \rho_1(x_1)$ maps $\check{x}_1 \in [L_1, \infty)$ to $x_1 \in [L_1, L_1 + d_1)$. As a result, the trapezoid Ω^r on the right is compressed along radial direction

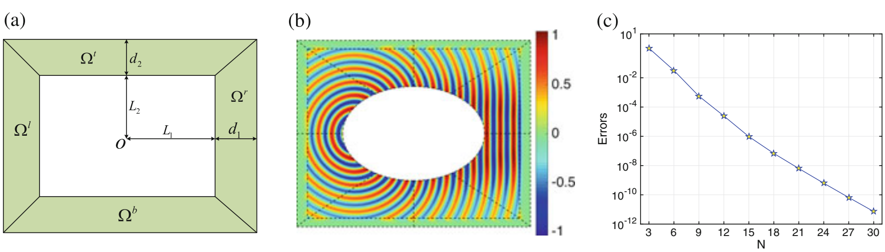

Fig. 5 In (b)–(c), $\partial D := \{(x, y) = \zeta(\cosh\xi \cos\theta, \sinh\xi \sin\theta), \theta \in [0, 2\pi)\}$ with $(\zeta, \xi) = (0.8, 0.5)$, $\sigma_0 = 1.5$. (**a**) Schematic illustration of $\Omega_{\rm ab}$. (**b**) ${\rm Re}(u_{\mathbf{N}})$ and ${\rm Re}(v_{\mathbf{N}})$. (**c**) Error of (a) against N

from an open "trapezoid" with $L_1 \le \breve{x}_1 < \infty$ and two infinitely-long, non-parallel sides on the same rays as Ω^r. Likewise for three other trapezoidal pieces, they are compressed from open "trapezoids".

Using Lemma 1, we can derive the Helmholtz-type PDE as with that in Theorem 1. Thanks to the symmetry of the layer, one only needs to calculate the material parameters in Ω^r and Ω^t.

Theorem 4 *By the transformation* (42)–(43)*, we have* $\mathbf{C}$ *and* $\mathbf{n}$ *take the form*

$$C_{11} = \frac{\beta_1}{\alpha}\frac{\rho_1}{x_1\rho_1'}, \quad C_{22} = \frac{\alpha}{\beta_1}\frac{x_1\rho_1'}{\rho_1} + \frac{\beta_1}{\alpha}\frac{\rho_1\rho_1'}{x_1}\Big(\frac{x_2}{x_1}\Big)^2\Big(\frac{1}{\rho_1'} - \frac{\alpha}{\beta_1}\frac{x_1}{\rho_1}\Big)^2, \tag{47a}$$

$$C_{12} = \frac{x_2}{x_1}\Big(\frac{\beta_1}{\alpha}\frac{\rho_1}{x_1\rho_1'} - 1\Big), \quad n = \alpha\beta_1\frac{\rho_1\rho_1'}{x_1}, \quad \text{in } \Omega^r, \tag{47b}$$

and

$$C_{11} = \frac{\alpha}{\beta_2}\frac{x_2\rho_2'}{\rho_2} + \frac{\beta_2}{\alpha}\frac{\rho_2\rho_2'}{x_2}\Big(\frac{x_1}{x_2}\Big)^2\Big(\frac{1}{\rho_2'} - \frac{\alpha}{\beta_2}\frac{x_2}{\rho_2}\Big)^2, \quad C_{22} = \frac{\beta_2}{\alpha}\frac{\rho_2}{x_2\rho_2'}, \tag{48a}$$

$$C_{12} = \frac{x_1}{x_2}\Big(\frac{\beta_2}{\alpha}\frac{\rho_2}{x_2\rho_2'} - 1\Big), \quad n = \alpha\beta_2\frac{\rho_2\rho_2'}{x_2}, \quad \text{in } \Omega^t, \tag{48b}$$

where $\alpha = 1 + \sigma_0\mathrm{i}$, *and* $\beta_i = \tilde{x}_i/\rho_i$ $(i = 1, 2)$. *With the symmetric relations* (44)–(45)*, we have*

$$\{C_{11}, C_{22}, n\}(x_1, x_2)|_{\Omega^l} = \{C_{11}, C_{22}, n\}(-x_1, x_2)|_{\Omega^r}, \;\; C_{12}(x_1, x_2)|_{\Omega^l} = -C_{12}(-x_1, x_2)|_{\Omega^r}, \tag{49}$$

$$\{C_{11}, C_{22}, n\}(x_1, x_2)|_{\Omega^b} = \{C_{11}, C_{22}, n\}(x_1, -x_2)|_{\Omega^t}, \;\; C_{12}(x_1, x_2)|_{\Omega^t} = -C_{12}(x_1, -x_2)|_{\Omega^t}. \tag{50}$$

We shall provide the derivations in a forthcoming work. Like (20), we use the following substitution to diminish the singularity and essential oscillations:

$$u = vw, \quad w = \big(L_1/\rho_1\big)^{3/2} e^{\mathrm{i}k\frac{r}{x_1}(\rho_1 - L_1)} \text{ in } \Omega^r, \;\; w = \big(L_2/\rho_2\big)^{3/2} e^{\mathrm{i}k\frac{r}{x_2}(\rho_2 - L_2)} \text{ in } \Omega^t, \tag{51}$$

$$w(x_1, x_2)|_{\Omega^l} = w(-x_1, x_2)|_{\Omega^r}, \;\; w(x_1, x_2)|_{\Omega^b} = w(x_1, -x_2)|_{\Omega^t}, \;\; \text{with } r = \sqrt{x_1^2 + x_2^2}. \tag{52}$$

This can be implemented as in Theorem 2. The details shall be reported in a later work.

To test our proposed method, we enclose the same elliptical scatterer with the same setting as in Fig. 3e by a rectangular layer with $(L_1, L_2) = (1, 0.8)$ and $(d_1, d_2) = (0.1, 0.08)$. We partition $\Omega = \{\Omega_f^{(i)}\}_{i=1}^8 \cup \{\Omega_{\rm ab}^{(i)}\}_{i=1}^8$ into 16 non-overlapping quadrilateral elements as shown in Fig. 5b. Once again, the spectral-element scheme can be implemented by the unconventional basis in (21) and $u_{\mathbf{N}} \in V_{\mathbf{N}}$ in (40) with w defined in (51)–(52). Let $\theta_0 = 0$, $k = 50$, and $\sigma_0 = 1.5$, we plot $\mathrm{Re}(u_{\mathbf{N}})|_{\Omega_f}$ and $\mathrm{Re}(v_{\mathbf{N}})|_{\Omega_{\mathrm{ab}}}$ with $(N_1, N) = (60, 30)$ in Fig. 5b. We plot the maximum error in Ω_f with fixed $N_1 = 60$ and $N = 3, 6, \cdots, 30$ in Fig. 5c. Observe that the error decays exponentially as N increases, and the approximation in the layer has no oscillation and is well-behaved.

4 Extensions and Discussions

We discuss various extensions and relevant futures works to conclude this report.

- The complex compression coordinate transformation (14) can be directly applied to construct three-dimensional spherical absorbing layer. However, the substitution (20) should be replaced by

$$u = vw, \quad w = \left(\frac{a}{\rho}\right)^2 e^{\mathrm{i}k(\rho - a)}. \tag{53}$$

- For 3D polyhedral layers, we can compress the outgoing waves of the open space in radial direction as with the polygonal layer outlined previously. The related real compression transformation can also be viewed as an inside-out polyhedral cloak version of that for the polyhedral cloak in [16].
- It is of interest and necessity to theoretically analyse the well-posedness of the reduced problem, and conduct the related error estimates, which the analysis in [7, 8, 15] can shed light on, and we shall report in future works.
- Time-dependent formulations of the equation in the absorbing layer can be obtained by taking the inverse Fourier transform in time of the time-harmonic counterparts as with the PML technique, see e.g., [9]. Remarkably, Daniel et al. in [2] proposed a high-order super-grid-scale absorbing layer, whose limiting case can be viewed as the real compression mapping discussed in Sect. 2.1, together with an artificial viscosity term to damp the waves. Different from the PAL technique and the above idea, which only involve spatial coordinate transformations, Zenginoğlu constructed a hyperboloidal layer in [17] by using a space-time coordinate transformation along characteristic lines. The comparison of the accuracy and efficiency between these methods is worthy of deep investigation.

Acknowledgements The authors thank Dr. Bo Wang from Hunan Normal University, China, for discussions at the early stage of this topic. L. Wang would like to thank the Scientific Committee and local organizers of ICOSAHOM 2016 for the conference invitation to Rio de Janeiro, Brazil. The work of two authors was partially supported by Singapore MOE AcRF Tier 1 Grant (RG 27/15) and MOE AcRF Tier 2 Grant (MOE 2013-T2-1-095, ARC 44/13).

Appendix 1. Proof of Theorem 1

Proof Given the transformation (14), (8) becomes

$$\mathbf{J} = \frac{\partial(x,y)}{\partial(\tilde{x},\tilde{y})} = \frac{\partial(x,y)}{\partial(r,\theta)}\frac{\partial(r,\theta)}{\partial(\tilde{\rho},\theta)}\frac{\partial(\tilde{\rho},\theta)}{\partial(\tilde{x},\tilde{y})}. \tag{54}$$

With $\tilde{\rho}$ in place of ρ in (9)–(10), we have

$$\mathbf{J} = \mathbf{R}\,\mathbf{J}_1\mathbf{R}^t \quad \text{with} \quad \mathbf{J}_1 = \begin{bmatrix} dr/d\tilde{\rho} & 0 \\ 0 & r/\tilde{\rho} \end{bmatrix}, \tag{55}$$

and

$$\mathbf{C} = \mathbf{R}\begin{bmatrix} c & 0 \\ 0 & 1/c \end{bmatrix}\mathbf{R}^t, \quad n = \frac{\tilde{\rho}}{r}\frac{d\tilde{\rho}}{dr} = \alpha\beta\frac{\rho}{r}\frac{d\rho}{dr}, \quad c := \frac{\tilde{\rho}}{r}\frac{dr}{d\tilde{\rho}} = \frac{\beta}{\alpha}\frac{\rho}{r}\frac{dr}{d\rho}. \tag{56}$$

Then we can work out the explicit expressions of n, c in (18) as (13).

Note that the asymptotic boundary condition at $r = b$ is transformed from the Sommerfeld radiation condition in (1b).

We now derive the estimate (19). For this purpose, we expand the solution and data in Fourier series:

$$\{u, \Psi\} = \sum_{|m|=0}^{\infty} \{\hat{u}_m(r), \hat{\psi}_m(r)\}e^{im\theta}, \tag{57}$$

where $\{\hat{u}_m(r), \hat{\psi}_m(r)\}$ are the Fourier coefficients. Then we can reduce the problem (16)–(17) to

$$\frac{1}{r}\big(rc\,\hat{u}_m'\big)' - \frac{m^2}{r^2c}\hat{u}_m + k^2 n\,\hat{u}_m = 0, \quad r \in [a,b), \quad |m| = 0,1,2,\cdots, \tag{58}$$

$$\hat{u}_m = \hat{\psi}_m \ \text{ at } \ r = a; \quad \frac{1}{\alpha}\frac{dr}{d\rho}\hat{u}_m' - \mathrm{i}ku = o(|\tilde{\rho}|^{-1/2}) \ \text{ as } \ r \to b^-. \tag{59}$$

One can verify by using the Bessel equation of Hankel function (cf. [1]):

$$r^2y'' + ry' + (r^2 - m^2)y = 0, \quad y = H_m^{(1)}(r),$$

that the unique solution of (16)–(17) is

$$u = \sum_{|m|=0}^{\infty} \hat{u}_m(r)e^{im\theta} \ \text{ with } \ \hat{u}_m(r) = \hat{\psi}_m\frac{H_m^{(1)}(k\tilde{\rho})}{H_m^{(1)}(ka)}. \tag{60}$$

We next resort to a uniform estimate of Hankel functions first derived in [7, Lemma 2.2]: *For any complex* z *with* $\mathrm{Re}(z), \mathrm{Im}(z) \geq 0$, *and for any real* Θ *such that* $0 < \Theta \leq |z|$, *we have for any real order* ν,

$$|H_\nu^{(1)}(z)| \leq e^{-\mathrm{Im}(z)\left(1-\frac{\Theta^2}{|z|^2}\right)^{1/2}} |H_\nu^{(1)}(\Theta)|, \tag{61}$$

which implies

$$\max_{|m|\geq 0} \left| \frac{H_m^{(1)}(k\tilde{\rho})}{H_m^{(1)}(ka)} \right| \leq \exp\Big\{-k\sigma_0(\rho-a)\Big(1-\frac{a^2}{k^2\rho^2+k^2\sigma_0^2(\rho-a)^2}\Big)^{1/2}\Big\}, \quad \rho > a. \tag{62}$$

Therefore, we can derive (19) by using the Parseval's identity of Fourier series and (62). □

Appendix 2. Proof of Theorem 2

Proof We first deal with the boundary term $\langle \mathbf{C}\nabla u \cdot \mathbf{n}, \phi\rangle_{\Gamma_b}$ in (24). By a direct calculation and (56), we have

$$(\partial_r u, r^{-1}\partial_\theta u)^t = \mathbf{R}^t \nabla u, \quad \mathbf{C}\nabla u \cdot \mathbf{n} = \mathbf{R}\,\mathrm{diag}(c, c^{-1})\,\mathbf{R}^t\,\nabla u \cdot \mathbf{n} = c\,\partial_r u. \tag{63}$$

Thus, using (56) and the substitutions: $\phi = w\psi$ and $u = wv$, we can write

$$\begin{aligned}
\langle \mathbf{C}\nabla u \cdot \mathbf{n}, \phi\rangle_{\Gamma_b} &= \langle c u_r, \phi\rangle_{\Gamma_b} = \langle c\bar{w} u_r, \psi\rangle_{\Gamma_b} = a^{3/2}\Big\langle \frac{\beta}{r}\sqrt{\frac{b-r}{s(r)}} e^{-\mathrm{i}k(\rho-a)} \frac{1}{\alpha}\frac{dr}{d\rho} u_r, \psi\Big\rangle_{\Gamma_b} \\
&= a^{3/2}\Big\langle \frac{\beta}{r}\sqrt{\frac{b-r}{s(r)}} e^{-\mathrm{i}k(\rho-a)} \Big(\frac{1}{\alpha}\frac{dr}{d\rho} u_r - \mathrm{i}ku\Big), \psi\Big\rangle_{\Gamma_b} + \mathrm{i}ka^{3/2}\Big\langle \frac{\beta}{r}\sqrt{\frac{b-r}{s(r)}} e^{-\mathrm{i}k(\rho-a)} u, \psi\Big\rangle_{\Gamma_b} \\
&= a^{3/2}\Big\langle \frac{\beta}{r}\sqrt{\frac{b-r}{s(r)}} e^{-\mathrm{i}k(\rho-a)} \Big(\frac{1}{\alpha}\frac{dr}{d\rho} u_r - \mathrm{i}ku\Big), \psi\Big\rangle_{\Gamma_b} + \mathrm{i}ka^3\Big\langle \frac{\beta}{r}\frac{(b-r)^2}{s^2(r)} v, \psi\Big\rangle_{\Gamma_b}.
\end{aligned}$$

Noting that the integral along Γ_b is in θ, we obtain from the transformed Sommerfeld radiation condition (17) that $\langle \mathbf{C}\nabla u \cdot \mathbf{n}, \phi\rangle_{\Gamma_b} \to 0$ as $r \to b^-$.

We next deal with the other two terms in (24). Using the basic differentiation rules

$$\nabla u = w\,\nabla v + v\,\nabla w, \quad \nabla\bar{\phi} = \bar{w}\,\nabla\bar{\psi} + \bar{\psi}\,\nabla\bar{w},$$

we derive from (24) and a direct calculation that

$$\mathbb{B}_{\Omega_{\rm ab}}(u,\phi) = \big(|w|^2\mathbf{C}\nabla v, \nabla\psi\big)_{\Omega_{\rm ab}} + \big(w\,\mathbf{C}\nabla v\cdot\nabla\bar w, \psi\big)_{\Omega_{\rm ab}} + \big(v\,\bar w\mathbf{C}\,\nabla w, \nabla\psi\big)_{\Omega_{\rm ab}} \\ + \big(\mathbf{C}\,\nabla w\cdot\nabla\bar w\, v, \psi\big)_{\Omega_{\rm ab}} - k^2\big(|w|^2\, n\, v, \psi\big)_{\Omega_{\rm ab}}. \tag{64}$$

As $\mathbf{C}$ is symmetric, one verifies readily that for any vectors $\mathbf{a}$ and $\mathbf{b}$ with two components, we have $(\mathbf{Ca})\cdot\mathbf{b} = (\mathbf{Cb})\cdot\mathbf{a}$. Thus, we can rewrite

$$\big(w\,\mathbf{C}\nabla v\cdot\nabla\bar w, \psi\big)_{\Omega_{\rm ab}} = \big(w\,\mathbf{C}\nabla\bar w\cdot\nabla v, \psi\big)_{\Omega_{\rm ab}}. \tag{65}$$

As w is independent of θ, we immediately get $\nabla w = \frac{dw}{dr}\mathbf{n}$. Then by (56),

$$\mathbf{C}\nabla w = \frac{dw}{dr}\mathbf{R}\,{\rm diag}(c, c^{-1})\,\mathbf{R}^t\,\mathbf{n} = c\frac{dw}{dr}\mathbf{n}. \tag{66}$$

Thus, we have

$$w\mathbf{C}\nabla\bar w = c\,w\frac{d\bar w}{dr}\mathbf{n}, \quad \bar w\mathbf{C}\nabla w = c\,\bar w\frac{dw}{dr}\mathbf{n}, \quad \mathbf{C}\,\nabla w\cdot\nabla\bar w = c\Big|\frac{dw}{dr}\Big|^2. \tag{67}$$

Introducing

$$\varpi_1 = |w|^2, \quad \varpi_2 = c\,\bar w\frac{\alpha}{\beta}\frac{dw}{dr}, \quad \varpi_3 = c\Big|\frac{dw}{dr}\Big|^2 - k^2|w|^2 n, \quad \partial_{\mathbf{n}} = \mathbf{n}\cdot\nabla, \tag{68}$$

we can derive (25) from (64)–(65) and (67)–(68). By (20),

$$\frac{dw}{dr} = w\frac{d\rho}{dr}\Big(-\frac{3}{2\rho} + {\rm i}k\Big). \tag{69}$$

We can work out $\{\varpi_j\}_{j=1}^3$ by using (12), (56) and (69). □

Appendix 3. Proof of Theorem 3

Proof We take $v = \psi$ in (25). By (56) and (63), we have

$${\rm Re}\big(\varpi_1\mathbf{C}\nabla v, \nabla v\big)_{\Omega_{\rm ab}} = {\rm Re}\int_0^{2\pi}\!\!\int_a^b \Big\{c|v_r|^2 + \frac{1}{cr^2}|v_\theta|^2\Big\}\varpi_1\, rdrd\theta \\ = \int_0^{2\pi}\!\!\int_a^b \Big\{{\rm Re}\Big(\frac{\beta}{\alpha}\Big)\frac{a^3}{r\rho^2}\frac{dr}{d\rho}\Big\}|v_r|^2 rdrd\theta + \int_0^{2\pi}\!\!\int_a^b \Big\{{\rm Re}\Big(\frac{\alpha}{\beta}\Big)\frac{a^3}{r\rho^4}\frac{d\rho}{dr}\Big\}|v_\theta|^2 rdrd\theta. \tag{70}$$

Using (26) and integration by parts leads to

$$
\begin{aligned}
&\mathrm{Re}\Big\{\frac{1}{\alpha}\big(\beta D_{\mathbf{n}}v, v\varpi_2\big)_{\Omega_{\mathrm{ab}}} + \frac{1}{\alpha}\big(\beta v\varpi_2, D_{\mathbf{n}}v\big)_{\Omega_{\mathrm{ab}}}\Big\} = 2\int_0^{2\pi}\!\!\int_a^b \mathrm{Re}\Big(\frac{\beta}{\alpha}\Big)\,\mathrm{Re}(\varpi_2 v\bar{v}_r)rdrd\theta \\
&= \int_0^{2\pi}\!\!\int_a^b \mathrm{Re}\Big(\frac{\beta}{\alpha}\Big)\,\mathrm{Re}(\varpi_2)(\partial_r|v|^2)rdrd\theta - 2\int_0^{2\pi}\!\!\int_a^b \mathrm{Re}\Big(\frac{\beta}{\alpha}\Big)\,\mathrm{Im}(\varpi_2)\mathrm{Im}(v\bar{v}_r)rdrd\theta \\
&= \frac{3}{2}\frac{1}{1+\sigma_0^2}\|v(a,\cdot)\|^2_{L^2(0,2\pi)} + \frac{3}{2}\int_0^{2\pi}\!\!\int_a^b \Big\{\frac{a^3}{r\rho^4}\Big(\frac{4\sigma_0^2}{1+\sigma_0^2}\frac{a}{\rho} - 3\Big)\frac{d\rho}{dr}\Big\}|v|^2 rdrd\theta \\
&\quad - 2k\int_0^{2\pi}\!\!\int_a^b \mathrm{Re}\Big(\frac{\beta}{\alpha}\Big)\frac{a^3}{\rho^2}\mathrm{Im}(v\bar{v}_r)drd\theta.
\end{aligned}
\tag{71}
$$

It is evident that

$$
\mathrm{Re}\big(\varpi_3 v, v\big)_{\Omega_{\mathrm{ab}}} = \int_0^{2\pi}\!\!\int_a^b \mathrm{Re}(\varpi_3)|v|^2 rdrd\theta. \tag{72}
$$

Note from (15) that

$$
\mathrm{Re}\Big(\frac{\beta}{\alpha}\Big) = 1 - \frac{\sigma_0^2}{1+\sigma_0^2}\frac{a}{\rho} > \frac{1}{1+\sigma_0^2}, \quad \mathrm{Re}\Big(\frac{\alpha}{\beta}\Big) = 1 + \frac{\sigma_0(1-a/\rho)}{1+\sigma_0^2(1-a/\rho)^2}\frac{a}{\rho} > 1. \tag{73}
$$

Using the Cauchy-Schwarz inequality, we obtain

$$
\begin{aligned}
2k\int_0^{2\pi}\!\!\int_a^b \mathrm{Re}\Big(\frac{\beta}{\alpha}\Big)\frac{a^3}{\rho^2}\mathrm{Im}(v\bar{v}_r)drd\theta \le \frac{1}{\epsilon}\int_0^{2\pi}\!\!\int_a^b \Big\{\mathrm{Re}\Big(\frac{\beta}{\alpha}\Big)\frac{a^3}{r\rho^2}\frac{dr}{d\rho}\Big\}|v_r|^2 rdrd\theta \\
+ \epsilon k^2\int_0^{2\pi}\!\!\int_a^b \Big\{\mathrm{Re}\Big(\frac{\beta}{\alpha}\Big)\frac{a^3}{r\rho^2}\frac{d\rho}{dr}\Big\}|v|^2 rdrd\theta,
\end{aligned}
\tag{74}
$$

where ϵ is a positive constant independent of k. Thus, by (25), (70)–(74) and collecting the terms, we obtain

$$
\begin{aligned}
\mathrm{Re}\big\{\mathbb{B}_{\Omega_{\mathrm{ab}}}(u,u)\big\} &\ge \Big(1-\frac{1}{\epsilon}\Big)\int_0^{2\pi}\!\!\int_a^b \Big\{\mathrm{Re}\Big(\frac{\beta}{\alpha}\Big)\frac{a^3}{r\rho^2}\frac{dr}{d\rho}\Big\}|v_r|^2 rdrd\theta \\
&+ \int_0^{2\pi}\!\!\int_a^b \Big\{\mathrm{Re}\Big(\frac{\alpha}{\beta}\Big)\frac{a^3}{r\rho^4}\frac{d\rho}{dr}\Big\}|v_\theta|^2 rdrd\theta + \frac{3}{2}\frac{1}{1+\sigma_0^2}\|v(a,\cdot)\|^2_{L^2(0,2\pi)} \\
&+ \int_0^{2\pi}\!\!\int_a^b \Big\{\mathrm{Re}(\varpi_3) + \Big(\frac{3}{2}\frac{1}{\rho^2}\Big(\frac{4\sigma_0^2}{1+\sigma_0^2}\frac{a}{\rho} - 3\Big) - \epsilon k^2\mathrm{Re}\Big(\frac{\beta}{\alpha}\Big)\Big)\frac{a^3}{r\rho^2}\frac{d\rho}{dr}\Big\}|v|^2 rdrd\theta.
\end{aligned}
\tag{75}
$$

We next work out and estimate the functions in the brackets. We have

$$s(r) = a^2 + r(b-2a) \leq |I|\bar{c}, \quad \bar{c} := \max\{a, |I|\}, \quad |I| := b-a. \tag{76}$$

By (12), (26) and (76),

$$\frac{a^3}{r\rho^2}\frac{dr}{d\rho} = \frac{a^3}{|I|^2}\frac{(b-r)^4}{rs^2(r)} \geq \frac{a^3}{b\,\bar{c}^2|I|^4}(b-r)^4; \quad \frac{a^3}{r\rho^4}\frac{d\rho}{dr} = \frac{a^3|I|^2}{r}\frac{(b-r)^2}{s^4(r)} \geq \frac{a^3}{b\,\bar{c}^4|I|^2}(b-r)^2, \tag{77}$$

so we can obtain the lower bounds of the first two terms.

With a careful calculation, we can work out the summation in the curly brackets of the last term in (75) by using (12), (15) and (26). □

References

1. M. Abramowitz, I.A. Stegun, (eds.) *Handbook of Mathematical Functions with Formulas, Graphs, and Mathematical Tables*. A Wiley-Interscience Publication (John Wiley & Sons Inc., New York, 1984). Reprint of the 1972 edition, Selected Government Publications.
2. D. Appelö, T. Colonius, A high-order super-grid-scale absorbing layer and its application to linear hyperbolic systems. J. Comput. Phys. **228**(11), 4200–4217 (2009)
3. J.P. Berenger, A perfectly matched layer for the absorption of electromagnetic waves. J. Comput. Phys. **114**(2), 185–200 (1994)
4. A. Bermúdez, L. Hervella-Nieto, A. Prieto, R. Rodríguez, An exact bounded perfectly matched layer for time-harmonic scattering problems. SIAM J. Sci. Comput. **30**(1), 312–338 (2007)
5. A. Bermúdez, L. Hervella-Nieto, A. Prieto, R. Rodríguez, An optimal perfectly matched layer with unbounded absorbing function for time-harmonic acoustic scattering problems. J. Comput. Phys. **223**(2), 469–488 (2007)
6. J.P. Boyd, *Chebyshev and Fourier Spectral Methods*, 2nd en. (Dover Publications, Mineola, 2001)
7. Z.M. Chen, X.Z. Liu, An adaptive perfectly matched layer technique for time-harmonic scattering problems. SIAM J. Numer. Anal. **43**(2), 645–671 (2005)
8. Z.M. Chen, X.M. Wu, Long-time stability and convergence of the uniaxial perfectly matched layer method for time-domain acoustic scattering problems. SIAM J. Numer. Anal. **50**(5), 2632–2655 (2012)
9. W.C. Chew, W.H. Weedon, A 3D perfectly matched medium from modified Maxwell's equations with stretched coordinates. Microw. Opt. Technol. Lett. **7**(13), 599–604 (1994)
10. F. Collino, P. Monk, The perfectly matched layer in curvilinear coordinates. SIAM J. Sci. Comput. **19**(6), 2061–2090 (1998)
11. L. Demkowicz, J. Shen, A few new (?) facts about infinite elements. Comput. Methods Appl. Mech. Eng. **195**(29–32), 3572–3590 (2006)
12. T. Hagstrom, Radiation boundary conditions for the numerical simulation of waves, in *Acta Numerica, 1999*, vol. 8 (Cambridge University Press, Cambridge, 1999), pp. 47–106
13. S. Johnson, Notes on perfectly matched layers. Technical Report, Massachusetts Institute of Technology, Cambridge, MA (2010)
14. J. Shen, T. Tang, L.L. Wang, *Spectral Methods: Algorithms, Analysis and Applications*, Springer Series in Computational Mathematics, vol. 41 (Springer, Berlin, 2011)

15. L.L. Wang, B. Wang, X.D. Zhao, Fast and accurate computation of time-domain acoustic scattering problems with exact nonreflecting boundary conditions. SIAM J. Appl. Math. **72**(6), 1869–1898 (2012)
16. Z.G. Yang, L.L. Wang, Z.J. Rong, B. Wang, B.L. Zhang, Seamless integration of global Dirichlet-to-Neumann boundary condition and spectral elements for transformation electromagnetics. Comput. Methods Appl. Mech. Eng. **301**, 137–163 (2016)
17. A. Zenginoğlu, Hyperboloidal layers for hyperbolic equations on unbounded domains. J. Comput. Phys. **230**(6), 2286–2302 (2011)
18. N.A. Zharova, L.V. Shadrivov, Y.S. Kivshar, Inside-out electromagnetic cloaking. Opt. Express **16**(7), 4615–4620 (2008)